Microslit-embedded acoustic metasurface for bandpass filter shaped sound absorption

Okuzono, Takeshi

(Citation)
Acoustical Science and Technology,45(3):147-157

(Issue Date)
2024-05-01

(Resource Type)
journal article

(Version)
Version of Record

Acoust. Sci. & Tech. **45**, 3 (2024)

PAPER

Microslit-embedded acoustic metasurface for bandpass filter shaped sound absorption

Takeshi Okuzono*

Environmental Acoustics Laboratory, Department of Architecture, Graduate School of Engineering, Kobe University, 1–1 Rokkodai, Nada, Kobe, 657–8501 Japan

(*Received 11 September 2023, Accepted for publication 26 December 2023*)

Abstract: This paper presents a proposal of sub-wavelength acoustic metasurface (AMS) sound absorbers, designated as MeAMS absorbers, with coupled-microslit resonators of gradually decreasing sizes in the respective component resonators. A MeAMS absorber can provide bandpass filter-shaped near-perfect absorption. The prediction theory of the present AMS absorbers is also proposed with two design methods to ascertain the dimensions of respective component resonators. The theory for AMS absorbers composed of single-microslit resonators is first verified with finite element method (FEM) simulation using thermoviscous boundary layer impedance boundary conditions. It is validated further for two 3D printed samples by an impedance tube measurement. Then, the theoretical predictability of absorption characteristics of MeAMS absorbers is discussed via FEM simulations and the impedance tube measurement for three 3D printed samples, revealing that the present theory provides a reasonable approximation of the absorption characteristics of MeAMS absorbers. Two one-third octave band near-perfect absorbers are also presented for practical applications.

Keywords: Acoustic metasurface, Coupled resonators, Microslit, Perfect absorption

1. INTRODUCTION

In recent years, acoustic metamaterial (AMM) absorbers and acoustic metasurface (AMS) absorbers have attracted considerable interest for use as sound absorbers to provide near-perfect absorption at low frequencies with sub-wavelength thickness and with the capability of sound absorption tunability on demand. Some valuable reviews [1,2] have elucidated recent progress in this field. A recent topic related to AMM and AMS absorbers is developing broadband highly efficient absorbers based on coupled resonator structures with sub-wavelength thickness because single resonator-based AMM and AMS absorbers have a narrow working frequency range. Two design strategies have been used to construct broadband AMS absorbers to date. By the first strategy, broadband near-perfect absorption is achieved using near-perfect absorption of each resonator. A labyrinthine AMS with multichannel [3] uses this strategy. The second strategy uses weak resonance coupling effects among resonators [1,4], by which respective resonators have low absorption peaks far from perfect absorption. The second strategy is used for AMS absorbers based on a neck-embedded Helmholtz resonator (NEHR) [4] and AMS absorbers based on cavity resonators with internally extended tubes (CRIET) with hexagonal honeycomb configuration [5]. Actually, AMS absorbers with multiple folded extremely long necks have also been designed as described for an earlier study [6] for broadband low-frequency absorption. Other attractive AMM absorbers are exemplified by metaporous material absorbers [7,8] and the sonic black hole absorbers [9,10].

Among various AMM and AMS absorbers, the study described herein specifically examines AMS absorbers based on microslit resonators [11–15] because the slit structure is easy to manufacture at low cost. Coupled microslit absorbers using two resonators were proposed in an earlier report [11,12]. Other recent attractive microslit-based AMS absorbers include AMS with symmetrical coiled spaces and variable depth microslit [13], AMS absorbers with double coiled-up spaces [14] and AMS absorber including convoluted spaces behind a microslit structure [15]. The coiled-up and convoluted spaces provide sound absorption tunability for low frequencies in a single-resonator-based AMS absorber. Earlier studies [13,14] demonstrated broader absorption performance based on the first strategy theoretically and numerically for AMS absorbers composed of two resonators having different resonant frequencies. However, it remains a challenge to design coupled microslit-based AMS absorb-

*e-mail: okuzono@port.kobe-u.ac.jp
[doi:10.1250/ast.e23.59]

ers using multiple-component resonators that can achieve near-perfect sound absorption at wideband under a simple design methodology.

This paper presents a proposal of a simply designable AMS absorber based on coupled-microslit resonators, which can provide bandpass filter-shaped near-perfect sound absorption. The design principle of the absorber is based on the the first strategy that each component resonator works as a near-perfect absorber with different resonant frequencies, as used in the labyrinthine AMS with multichannel [3]. However, the present AMS absorber uses a different design method for each component resonator's dimension.

As one advantage, the present absorber's absorption characteristics can be predicted rapidly with a reasonable accuracy using a highly versatile theory applicable to AMS absorbers with holes of various shapes. In addition, the present absorbers can be fabricated easily because they have simple geometry.

The presentation of this study is organized as follows. Section 2 proposes the theory of the proposed AMS absorber based on the flow formulation-based transfer matrix method (TMM). Then, Sect. 3 presents verification of the theory for AMS absorber with a single-microslit resonator, which is a component resonator that constructs the proposed coupled microslit AMS absorbers with the numerical simulation by the finite element method (FEM). In Sect. 4, the theory for AMS absorber with a single-microslit resonator is validated further with an impedance tube measurement. Section 5 shows verification and validation studies of the proposed coupled microslit AMS absorbers using FEM and impedance tube measurements. The absorption mechanism of the absorber is also discussed theoretically and numerically. Section 6 concludes the discussion presented herein.

2. THEORY

Figure 1(a) portrays the present microslit-embedded AMS (MeAMS) absorber, a coupled-microslit resonator with gradually decreasing size in each resonator. The figure presents an example case with nine resonators. The number of resonators can be changed. In the MeAMS absorbers, i-th resonator has a_i period, H_i thickness, and b_0 wall thickness. Figure 1(b) presents examples of resonator design for $i = 1$, 2 and 3. The period and thickness are variable. Two design theories are proposed in this paper. In addition, each resonator has a neck-embedded slit of h_i $(= H_i)$ slit length, d_i slit width, and ls_i slit height. Furthermore, the air cavity behind the slit in each resonator has width w_i $(= H_i - 2b_0)$ and thickness l_i $(= a_i - 3b_0 - d_i)$. Symbol Δ_i $(= H_1 - H_i)$ represents the additional wall thickness for i-th resonator to keep a flat surface in the back wall. The absorption characteristics of the present MeAMS

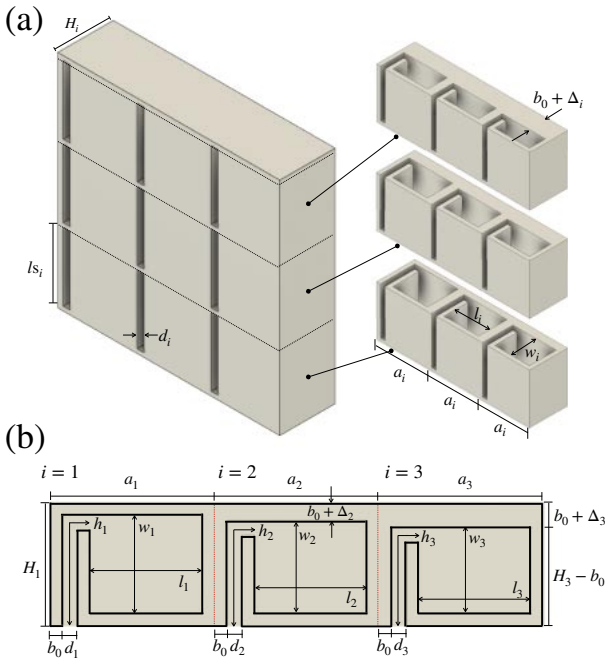

Fig. 1 MeAMS absorber with nine resonators: (a) 3D geometry model and (b) resonator design example for $i = 1$, 2 and 3.

absorber are predictable using TMM as described hereinafter. The presented TMM modeling is based on the author's earlier work [16] in micro-perforated plate modeling. An important benefit is that it is systematically applicable to various shaped micro-perforated holes such as a circle, a square, and a triangle, by changing the flow resistivity and equivalent radius of the hole.

2.1. Absorption Modeling of AMS with Single-microslit Resonator

First, we propose a theoretical acoustic impedance model of the SAMS absorber (Fig. 2), which is an AMS absorber composed of periodically located single-microslit

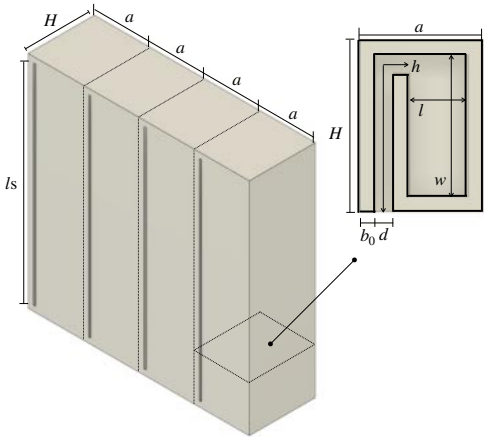

Fig. 2 SAMS absorber.

resonators in which the period and the thickness are characterized respectively by a and H. The thermoviscous losses attributable to the plane wave propagation inside the slit with $h\ (=H)$ length, d width, and ls height can be modeled using the following complex effective density ρ_e and the complex bulk modulus K_e as [17]

$$\rho_e = \rho_0\left[1 + \frac{\sigma\phi}{\mathrm{j}\omega\rho_0} G_c(s_1)\right], \tag{1}$$

$$K_e = \frac{\gamma P_0}{\gamma - (\gamma-1)F(\mathrm{Pr}\omega)}, \tag{2}$$

where ρ_0 stands for the air density, j denotes the imaginary unit, ω expresses the angular frequency, and $\sigma\phi$ signifies the flow resistivity of the hole. For the slit with the cross-sectional area S_s and the perimeter l_p, it is defined as $\sigma\phi = 12\eta/\bar{r}^2$. The equivalent radius $\bar{r}$ of the slit is given as $\bar{r}\ (= 2S_s/l_p)$. The parameter η denotes the air viscosity. Additionally, γ is the specific heat ratio, P_0 represents the atmospheric pressure, and Pr is the Prandtl number. The two functions $G_c(s_1)$ and $F(\mathrm{Pr}\omega)$ are given respectively with the parameter $s_1\ (= s\sqrt{-\mathrm{j}})$ as [17]

$$G_c(s_1) = -\frac{s_1}{4}\frac{J_1(s_1)}{J_0(s_1)}\left[1 - \frac{2}{s_1}\frac{J_1(s_1)}{J_0(s_1)}\right]^{-1}, \tag{3}$$

$$F(\mathrm{Pr}\omega) = \left[1 + \frac{\sigma\phi}{\mathrm{jPr}\omega\rho_0} G_c(s_1\sqrt{\mathrm{Pr}})\right]^{-1}, \tag{4}$$

where J_0 and J_1 respectively represent Bessel functions of the first kind on the zeroth and first orders. The parameter s, which includes the shape-dependent coefficient $c\ (= \sqrt{8\eta(\sigma\phi)^{-1}}/\bar{r})$ is defined as $s = c\sqrt{8\omega\rho_0(\sigma\phi)^{-1}}$. With the viscothermal dissipation modeling above, the transfer matrix of the slit $\boldsymbol{T}_s$ takes the form in the flow formulation as

$$\boldsymbol{T}_s = \begin{bmatrix} \cos(k_e h) & \mathrm{j}Z_c S_s^{-1}\sin(k_e h) \\ \mathrm{j}S_s Z_c^{-1}\sin(k_e h) & \cos(k_e h) \end{bmatrix}, \tag{5}$$

where $Z_c\ (= (\rho_e K_e)^{1/2})$ and $k_e\ (= \omega(\rho_e K_e^{-1})^{1/2})$ respectively represent the characteristic impedance and the complex wave number of the slit. The edge impedance Z_e of slits, which describes the resistive and reactive end corrections, is given as

$$Z_e = R + \mathrm{j}\omega\rho_0\frac{dF(e)}{2F(\epsilon)}, \tag{6}$$

where $R\ (= \sqrt{2\eta\rho_0\omega}/2)$ represent the surface resistance of the panel, $F(e)$ is the complete elliptical integral with the ellipticity of the surface $e\ (= \sqrt{1-(0.5d)^2/(0.5ls)^2})$ [18], and $F(\epsilon)$ is the Fok function with the parameter ϵ defined by the square root of the perforation ratio of the slit. $F(\epsilon)$ is given as [13,19,20]

$$\begin{aligned} F(\epsilon) = (1 &- 1.4092\epsilon + 0.33818\epsilon^3 + 0.06793\epsilon^5 \\ &- 0.02287\epsilon^6 + 0.03015\epsilon^7 - 0.01641\epsilon^8)^{-1}. \end{aligned} \tag{7}$$

The transfer matrix relevant to the end correction of slits $\boldsymbol{T}_e$ takes the form in the flow formulation as

$$\boldsymbol{T}_e = \begin{bmatrix} 1 & Z_e S_s^{-1} \\ 0 & 1 \end{bmatrix}. \tag{8}$$

Additionally, the transfer matrix of the air cavity with width w and thickness l behind slit $\boldsymbol{T}_c$ given as

$$\boldsymbol{T}_c = \begin{bmatrix} \cos(k_0 l) & \mathrm{j}Z_0 S_c^{-1}\sin(k_0 l) \\ \mathrm{j}S_c Z_0^{-1}\sin(k_0 l) & \cos(k_0 l) \end{bmatrix}, \tag{9}$$

where k_0 is the wave number of the air, S_c denotes the cross-sectional area of the air cavity, and Z_0 represents the characteristic impedance of the air. With the three transfer matrices above, the total transfer matrix of the SAMS absorber $\boldsymbol{T}_{\mathrm{SAMS}}$ is

$$\boldsymbol{T}_{\mathrm{SAMS}} = \boldsymbol{T}_e\boldsymbol{T}_s\boldsymbol{T}_c. \tag{10}$$

From the equation presented above, the sound pressure p_i and the volume velocity U_i on the absorber's surface can be related to the sound pressure p_e and the volume velocity U_e at the end of the absorber as

$$\begin{pmatrix} p_i \\ U_i \end{pmatrix} = \boldsymbol{T}_{\mathrm{SAMS}}\begin{pmatrix} p_e \\ U_e \end{pmatrix} = \begin{bmatrix} t_{11} & t_{12} \\ t_{21} & t_{22} \end{bmatrix}\begin{pmatrix} p_e \\ U_e \end{pmatrix}. \tag{11}$$

The specific acoustic impedance of a rigidly backed SAMS absorber Z_{SAMS} is computed as $Z_{\mathrm{SAMS}} = S_i t_{11} t_{21}^{-1}$ with the boundary condition $U_e = 0$ at the end, where S_i represents the incidence surface area of the absorber.

2.2. Absorption Modeling of AMS Composed of Coupled-microslit Resonator

The specific acoustic impedance of MeAMS absorber Z_{MeAMS} is calculable using the admittance sum method as

$$Z_{\mathrm{MeAMS}} = \left(\sum r_i Z_{\mathrm{SAMS},i}^{-1}\right)^{-1}, \tag{12}$$

where $Z_{\mathrm{SAMS},i}$ is the specific acoustic impedance of i-th SAMS absorber with a different resonant frequency, and where r_i is the surface area ratio of the i-th SAMS absorber to the incidence surface area of MeAMS absorber.

We propose two design methods, designated as Method 1 and Method 2, to produce resonators with different resonant frequencies. In Method 1, the period of each resonator is set to a constant value as $a_i = a_1$. Each resonator's slit width and height are also constant as $d_i = d_1$ and $ls_i = ls_1$. Only the resonator thickness H_i should be decreased gradually according to function $H_i = H_1 - \Delta_i$ with $\Delta_i = (i-1)d_x$, where d_x is the parameter which determines the degree of thickness reduction and which gives tunability on absorption bandwidth to some extent. By contrast, Method 2 can be changed both the period a_i and the thickness H_i of each resonator while maintaining the slit width and height constant as $d_i = d_1$ and $ls_i = ls_1$.

Table 1 Specifications of seven SAMS absorbers and their theoretical and numerical resonant frequencies.

No	a, mm	d, mm	$f_{0,\mathrm{th}}$, Hz	$f_{0,\mathrm{FEM}}$, Hz
#1	400	2.2	126	126
#2	200	1.5	166	166
#3	133.3	1.4	204	204
#4	100	1.6	256	255
#5	33.3	0.9	358	360
#6	25	0.8	399	398
#7	16	0.7	490	488

The a_i and H_i are respectively determined as $a_i = a_1 - \Delta_i$ and $H_i = H_1 - \Delta_i$. For both design methods, the dimension of each component resonator is determined automatically once the first resonator dimension, which determines the lowest resonance frequency, is given together with parameter d_x.

3. VERIFICATION OF SAMS MODELING

This section verifies the theoretical impedance of the SAMS absorber with FEM in the frequency domain by COMSOL Multiphysics 6.1. We considered seven SAMS absorbers #1–#7, each of which has near-perfect absorption at a theoretical resonance frequency $f_{0,\mathrm{th}}$ at the center frequency of 1/3 octave band in 125–500 Hz. The values of b_0 and H are 1 mm and 25 mm for all absorbers. Table 1 presents the specifications of the seven absorbers, each with a different period and slit width, and their $f_{0,\mathrm{th}}$. The maximum and the minimum periods are, respectively, 400 mm for the absorber#1 with $f_{0,\mathrm{th}} = 126$ Hz and 16 mm for the absorber#7 with $f_{0,\mathrm{th}} = 490$ Hz. The slit width is in the range of 0.7–2.2 mm. The table includes numerical resonant frequencies $f_{0,\mathrm{FEM}}$ by FEM described in Sect. 3.1.

3.1. FEM Model of SAMS Absorber

Figures 3(a) and 3(b) respectively show a FEM model to compute the specific acoustic impedance Z_{FEM} and normal incidence absorption coefficient α_0. In the FEM model, the air region was modeled by the Helmholtz equation. Plane-wave incidence with unit amplitude and zero phase was modeled with the Background Pressure Field (BPF) interface [21] combined with Perfectly Matched Layer (PML) to absorb the scattered sound. In addition, Thermoviscous Boundary Layer Impedance (TBLI) condition [21,22] was assigned to model visco-thermal dissipations on slit surfaces and wall surfaces around the slit marked by pink lines in Fig. 3(b). The periodicity in the absorber was considered by the Periodic Condition (PC) interface [21]. Spatial discretization was performed by hexahedral and tetrahedral elements with second-order Lagrange functions. The hexahedral elements were used to discretize air domains in the slit and around

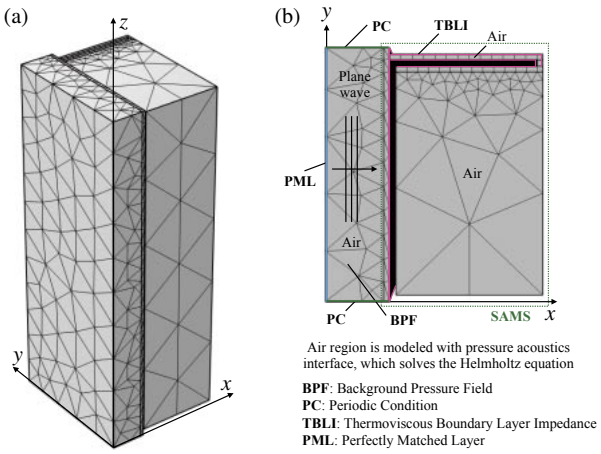

Fig. 3 FEM model of SAMS absorber: (a) 3D geometry model discretized with hexahedral and tetrahedral elements and (b) top view with numerical modeling in the sound field.

the slit with the maximum element size less than d. The remaining air domains were discretized using tetrahedral elements with a maximum element size of less than one-tenth of the 850 Hz wavelength. The used FEM mesh gives a convergent solution. The specific acoustic impedance of the absorbers was computed as

$$Z_{\mathrm{FEM}} = \frac{\dfrac{\int p \mathrm{d}S_{\mathrm{i}}}{\int \mathrm{d}S_{\mathrm{i}}}}{\dfrac{\int v_x \mathrm{d}S_{\mathrm{i}}}{\int \mathrm{d}S_{\mathrm{i}}}}, \tag{13}$$

where p and v_x respectively denote the sound pressure and particle velocity on the absorber's surface. The symbol $\int \cdot \mathrm{d}S_{\mathrm{i}}$ represents the surface integral.

3.2. Results and Discussion

Figure 4 compares α_0s of the seven absorbers #1–#7 computed by the theoretical impedance model and the FEM. It is apparent that the theoretical model matches the FEM well for all absorbers. Table 1 shows that the resonance frequencies $f_{0,\mathrm{th}}$ of the theoretical model agree well with the $f_{0,\mathrm{FEM}}$ of the FEM with the absolute error less than 2 Hz. Additionally, Fig. 4 demonstrates that the present SAMS absorber can achieve near-perfect absorption by control of the period and the slit width of the absorber with constant thickness of $H = 25$ mm. The wider period and slit width are necessary for perfect absorption at lower frequencies.

Figure 5 presents comparison of the specific acoustic impedance ratio of the seven absorbers #1 and #7 computed by the theoretical impedance model and the

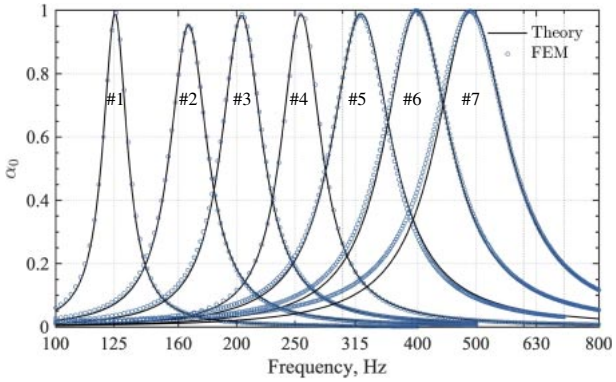

Fig. 4 Comparison of α_0 between theory and FEM for SAMS absorbers #1–#7.

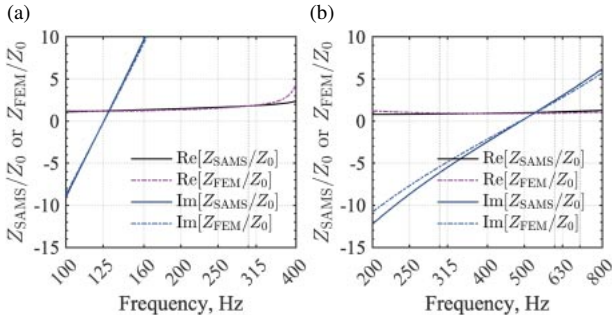

Fig. 5 Comparison of specific acoustic impedance ratio between theory (Z_{SAMS}/Z_0) and FEM (Z_{FEM}/Z_0) for SAMS absorbers (a) #1 and (b) #7.

FEM. The theoretical model agrees well with the FEM for both cases, showing that the presented impedance model has sufficient predictability of the absorption characteristics of SAMS absorbers. We also obtained good agreement for the remaining absorbers. The theoretical impedance model shows some discrepancies from the FEM in real and imaginary parts at frequencies away from the resonant frequency. This is probably true because the modeling of thermoviscous loss at the slit in the theory does not incorporate consideration of the bending of the slit.

4. VALIDATION OF SAMS MODELING

This section presents further validation of the theoretical impedance of the SAMS absorber using an impedance tube measurement with the transfer function method described in ISO 10534-2 [23]. We used an impedance tube with a 100 mm × 100 mm square cross-section and 500 mm length for the measurement, with measurement devices depicted in Fig. 6. The gap between samples and tube walls is sealed with tape. A pink noise was emitted from a loudspeaker (FW108N; FOSTEX Co., Ltd.) as a sound source via a power amplifier (Model1706II; BOSE Corp.). The transfer function H_{12} was measured using an FFT analyzer (SA-A1; RION Co., Ltd.) from sound

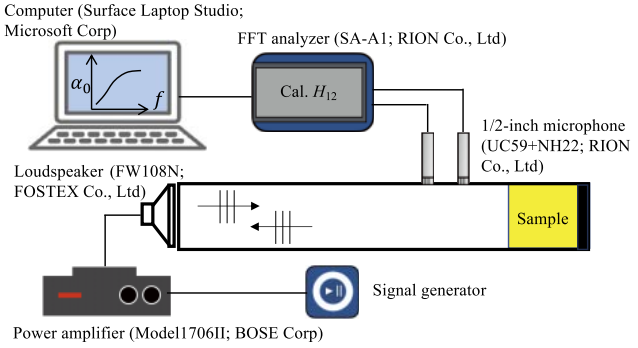

Fig. 6 A block diagram of measurement devices.

pressures measured by two 1/2-inch microphones (UC-59+NH22; RION Co., Ltd.). The microphone distance to a sample and microphones spacing follow ISO 10534-2 [23]. A microphone switching technique was used to correct microphone mismatch. The frequency resolution of FFT is 1.25 Hz. Averaging was performed 50 times in the frequency domain with a hanning window. The sound absorption characteristics were calculated from H_{12} using in-house MATLAB code. Measurements were performed in a soundproof room. Two SAMS absorbers, designated as Sample A1 and Sample A2, with different resonant frequencies fabricated using a 3D printer (Creator 3 Pro; FLASHFORGE), were examined after a preliminary experiment to elucidate the wall thickness b_0 of the absorber. The 3D printing method is based on fused deposition modeling using a PLA filament with density of $1.25 \pm 0.05\,\mathrm{g/cm^3}$. For manufacturing the present absorber, the wall thickness must be determined so that the absorber has a rigid skeleton. As a result, the two absorbers were fabricated with $b_0 = 2.5$ mm with 100% infill density. The absorber's size is 100 mm × 100 mm × H. Specifications of the two SAMS absorbers were the following: Sample A1 has $f_{0,\mathrm{th}} = 395$ Hz with the parameters of $a = 25$ mm, $H = 30$ mm, and Sample A2 has $f_{0,\mathrm{th}} = 509$ Hz with the parameters of $a = 20$ mm and $H = 28$ mm. The slit width and height of the two absorbers are the same as $d = 0.8$ mm and $ls = 95$ mm. Figure 7 portrays a photograph of 3D-printed samples of the two SAMS absorbers.

Figures 8(a) and 8(b) present comparison of the specific acoustic impedance ratio and the α_0 between the theoretical impedance model and the measurements for Sample A1 and Sample A2. The figure denotes the measured specific acoustic impedance ratio as Z_{Meas}/Z_0. Overall, the theoretical impedance model matches the measured values in both the specific acoustic impedance ratio and α_0. For Sample A1, the theoretical resonance frequency $f_{0,\mathrm{th}}$ is 395 Hz. It agrees with the measured resonance frequency $f_{0,\mathrm{meas}}$ of 389 Hz with absolute differ-

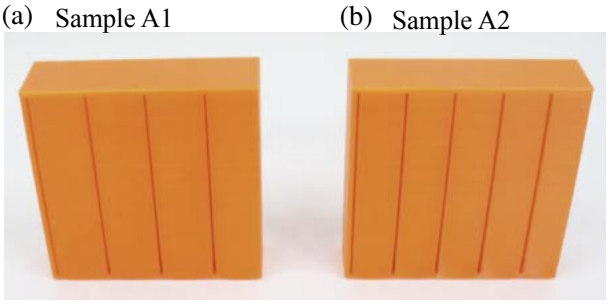

Fig. 7 Two 3D printed SAMS absorbers for validation: (a) Sample A1 and (b) Sample A2.

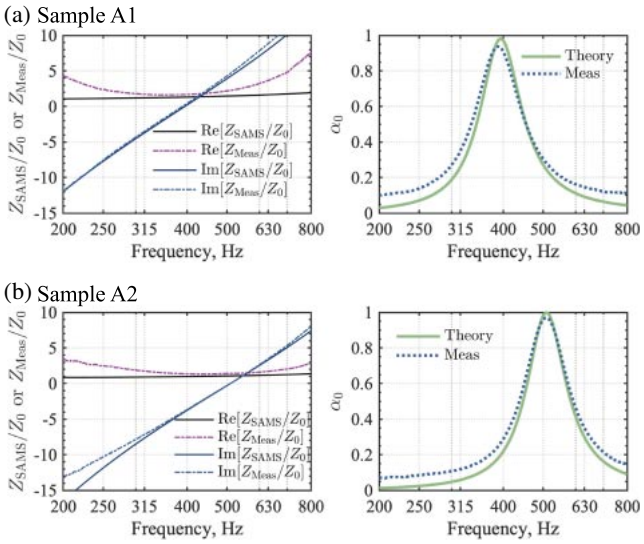

Fig. 8 Specific acoustic impedance ratios and α_0 found from theory and measurements: (a) Sample A1 and (b) Sample A2.

ence of 6 Hz. In addition, α_0 at $f_{0,\mathrm{th}}$ is 0.98, which differs slightly from the measured value of 0.94 at $f_{0,\mathrm{meas}}$. For Sample A2, we obtained better prediction accuracy than that for Sample A1. The $f_{0,\mathrm{th}}$ from the impedance model completely matches with $f_{0,\mathrm{meas}}$ of 509 Hz. The α_0 at $f_{0,\mathrm{th}}$ is 1.0, which is only 0.03 different from the measured value of 0.97. The results clearly revealed that the present SAMS absorber can be designed as a near-perfect sound absorber with the present impedance model.

We further show whether FEM provides more accurate prediction for Sample A1 and Sample A2 in Figs. 9(a) and 9(b). The results showed that FEM provides a similar level of prediction as in the present impedance model. The $f_{0,\mathrm{FEM}}$ for Sample A1 is 393 Hz, which is slightly better than the present impedance model with an absolute difference of 4 Hz. α_0 at $f_{0,\mathrm{FEM}}$ is 0.98, which is the same as in the present impedance model. For Sample A2, $f_{0,\mathrm{FEM}}$ is 507 Hz, which is a slightly lower value than $f_{0,\mathrm{th}}$ with the absolute difference of 2 Hz. The α_0 at $f_{0,\mathrm{th}}$ is 1.0 as in the present impedance model. From the results, we can say that

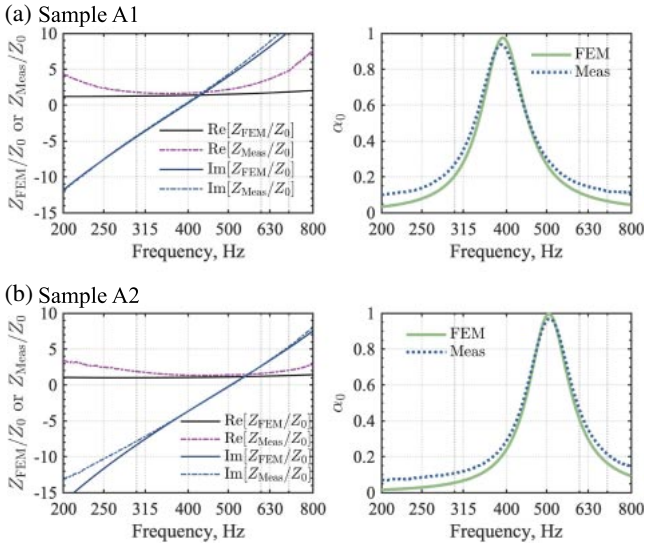

Fig. 9 Specific acoustic impedance ratios and α_0 found from FEM and measurements: (a) Sample A1 and (b) Sample A2.

the present impedance model at least has a similar level of accuracy as in FEM in predicting SAMS absorbers. Manufacturing accuracy in 3D printed samples, i.e., the dimension error in 3D printed samples, may be a reason for the slight discrepancies between the two prediction methods and the measurement. As is mentioned in earlier works [12,13,24] for microperforated panel absorbers and microslit panel absorbers, the difference of dimensions between predictions and measured samples may become a reason that explains the discrepancies between predictions and measurements. In this aspect, the precision of slit width is a critical parameter that affects the resulting resonant frequency for SAMS absorbers.

5. VERIFICATION AND VALIDATION OF MeAMS MODELING WITH ITS SOUND ABSORPTION MECHANISM

In this section, we first verify and validate the theoretical impedance model of the MeAMS absorber, which is designed by Method 1 and Method 2, using FEM and the impedance tube measurement. The absorption mechanism of the MeAMS absorbers is also explained from theoretical and numerical aspects. Practical absorbers for room acoustics applications will be designed in the last section. Three MeAMS absorbers were examined in Sects. 5.1, 5.2, and 5.3 to verify and validate the present theory. Two of the three absorbers were designed using Method 1, designated as Sample B1 and Sample B2. The remaining absorber was designed using Method 2 and was designated as Sample B3. Table 2 presents the specifications of the three MeAMS absorbers, where parameter n represents the number of resonators with different resonant

Table 2 Specifications of three MeAMS absorbers.

Sample	n	a_1 mm	H_1 mm	d_x mm	d_1 mm	ls_1 mm
B1	9	33.3	25	0.75	3.0	30.63
B2	9	33.3	25	1.2	3.0	30.63
B3	4	33.3	35	1.67	1.8	95

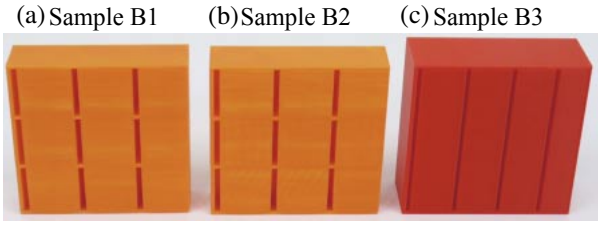

Fig. 10 Three 3D printed MeAMS absorbers for validation: (a) Sample B1, (b) Sample B2, and (c) Sample B3.

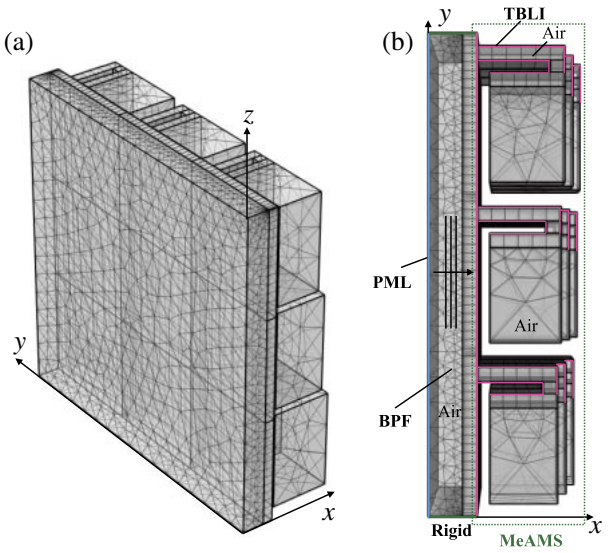

Fig. 11 FEM model of Sample B1: (a) 3D geometry model discretized with hexahedral and tetrahedral elements, (b) Top view with numerical modeling in the sound field.

frequencies. Samples B1 and B2 are MeAMS absorbers composed of nine SAMS absorbers with different resonant frequencies. Then they have the same dimensions, except for parameter d_x to control the bandwidth of absorption. Because they designed using Method 1, the nine resonators have the same period as a_1 and have different H_i, which is determined automatically by setting H_1 and d_x.

By contrast, Sample B3, designed by Method 2, is a MeAMS absorber composed of four resonators. The four resonators have different periods a_i and different H_i. All MeAMS absorbers have wall thickness b_0 of 2.5 mm. Figure 10 portrays a photograph of 3D-printed samples of the three MeAMS absorbers. The 3D printing technology is the same as in the preceding Sect. 4, using the same PLA filament with 100% infill density.

5.1. Verification with FEM

Figure 11 shows an example of FEM model of MeAMS absorber to compute Z_{FEM} and α_0. The modeling method is the same as used for SAMS absorber in Sect. 3.1. However, the side walls of the incident field were assumed to be a rigid boundary instead of the periodic condition used in SAMS modeling. Hexahedral and tetrahedral elements with second-order Lagrange functions were used for spatial discretization. The resulting mesh has a spatial resolution of ten elements per wavelength at 1,700 Hz. The Z_{FEM} of the MeAMS absorber was computed using Eq. (13).

Figures 12(a), 12(b), and 12(c) respectively compare the specific acoustic impedance ratio and α_0 between the theoretical impedance model and FEM for Sample B1, B2, and B3. Although some discrepancies exist in frequencies at which peaks and dips occur, the theoretical impedance

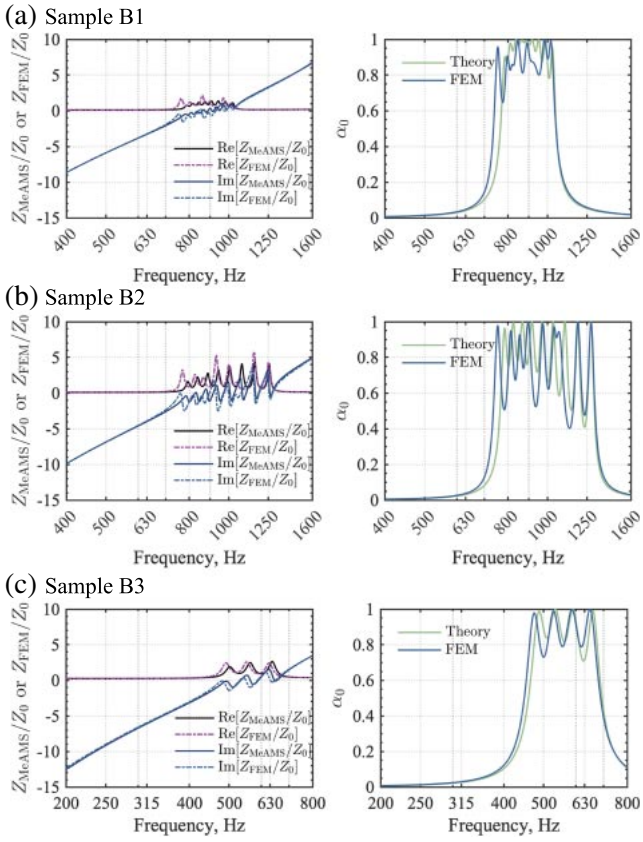

Fig. 12 Comparison of the specific acoustic impedance ratio and α_0 between theory and FEM: (a) Sample B1 (b) Sample B2, and (c) Sample B3.

model provides a reasonable prediction to FEM, showing the basic predictability of the absorption characteristics of MEAMS absorbers. We can find a better agreement for

Sample B3 with fewer resonators. The discrepancy in the absorption characteristics is because the present theoretical impedance model does not model the individual resonator's contribution to the overall absorption precisely where the effects arising from evanescent waves are not included [25]. Meanwhile, FEM models their contributions precisely. Since Sample B1 and B2 include coupling effects between nine resonators, each resonator's contribution to overall absorption is more complex than Sample B3. Therefore, the prediction accuracy of the theoretical impedance model in Sample B1 and B2 is reduced compared to that in Sample B3.

5.2. Validation with Impedance Tube Measurements

Figures 13(a), 13(b), and 13(c) respectively compare the specific acoustic impedance ratio and α_0 between the theoretical impedance model and the measurements for Sample B1, B2, and B3. As a reference, α_0 of FEM is also given in the figures. Results show that the present theoretical impedance model reasonably predicts the measured values, although it can not correctly consider the resonators' coupling. The present theoretical impedance model showed better agreement for Sample B3, which is consistent with the previous comparison results between FEM and the theoretical impedance model. This revealed that the present impedance model with two design methods, Method 1 and Method 2, can be used as a simple design method for MeAMS absorbers. On the other hand, FEM prediction gives fairly good agreement with the measured value for Sample B3 with fewer resonators. Its agreement at frequencies at which peaks and dips occur is better than that of the present theoretical impedance model, showing the validity of the present FEM predictions. Two additional peaks that are not confirmed in the FEM predictions and the theory appear at 710 Hz and 766.3 Hz in the measured value. This is probably due to the resonant vibration of the skeleton since the two prediction methods do not consider the structure-acoustic interaction. We will evaluate the effect of structure-acoustic interaction in future works. Although FEM predictions can consider the coupling among resonators naturally, they show a similar level of agreement to measurements as in the theoretical impedance model for Samples B1 and B2. The dimension errors in the samples made by 3D printers might be a possible reason for the discrepancies between FEM and measurements.

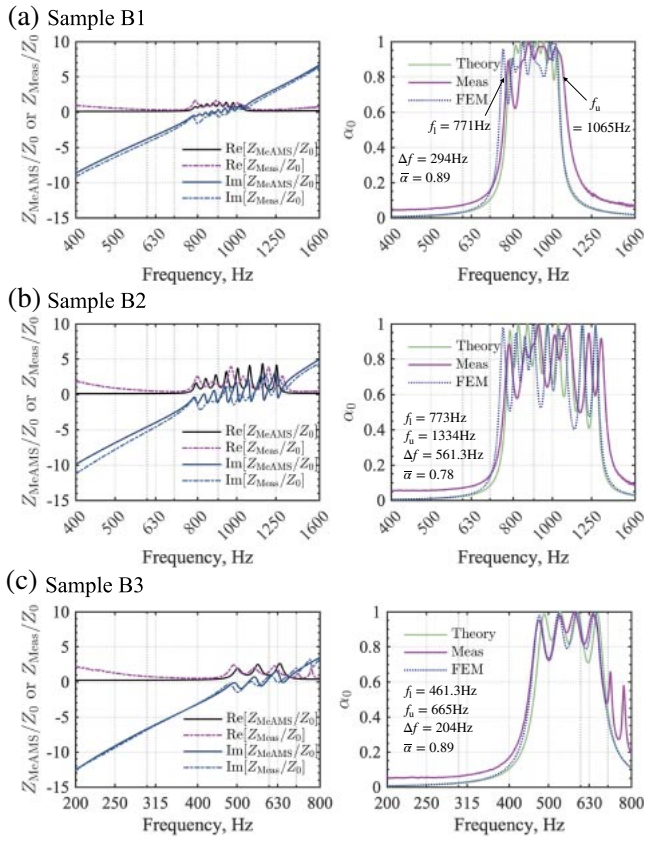

Fig. 13 Specific acoustic impedance ratios and α_0 found from theory and measurements: (a) Sample B1, (b) Sample B2, and (c) Sample B3. α_0 of FEM is shown as reference.

Regarding the absorption characteristics of the MeAMS absorbers, their bandpass filter-shaped absorption is readily apparent. In the figures of α_0, it is apparent that f_l and f_u respectively denote the lower limit frequency and the upper limit frequency: They are the first and last frequency at which α_0 exceeds 0.8 in the measured values. For Sample B1, f_l and f_u respectively denote 771 Hz and 1,065 Hz, and the effective bandwidth Δf, which is defined as $\Delta f = f_u - f_l$, is 294 Hz. Sample B1 has high absorption with the averaged normal-incidence absorption coefficient $\bar{\alpha}$ of 0.89 at the frequency range. We can find that Sample B2 has $\bar{\alpha}$ of 0.78 at frequencies of $f_l = 773$ Hz to $f_u = 1{,}334$ Hz. Also, Δf is 561 Hz. The effective bandwidth is greater than that of Sample B1, but $\bar{\alpha}$ becomes slightly lower than Sample B1 because the spacing between the resonance frequencies of the nine resonators in Sample B2 is more distant than in Sample B1, with a larger value of d_x. Therefore, the present MeAMS absorber has the tunability of effective bandwidth to some extent by parameter d_x for a given number of resonators. If one wants to obtain near-perfect absorption at all frequencies in the effective bandwidth, then the resonant frequency's spacing in resonators should be small to keep $\mathrm{Re}[Z_{\mathrm{MeAMS}}/Z_0] \simeq 1$ and $\mathrm{Im}[Z_{\mathrm{MeAMS}}/Z_0] \simeq 0$ as can be understood from the comparison of the specific acoustic impedance ratio of Figs. 13(a) and 13(b). This small spacing means that more resonators are necessary to construct a wider-band, near-perfect absorber. For Sample B3, we obtained $\bar{\alpha}$ of 0.89 in the frequencies of $f_l = 461.3$ Hz to $f_u = 665$ Hz. The Δf is 204 Hz.

5.3. Sound Absorption Mechanism

This section explains the underlying sound absorption mechanism of MeAMS absorbers designed by Method 1 and 2 from the theoretical and numerical aspects. In the present theory expressed by Eq. (12), it is assumed that i-th resonator in the MeAMS absorber works as a sound-absorbing surface with specific acoustic impedance $Z^i_{\mathrm{MeAMS}} = (r_i Z^{-1}_{\mathrm{SAMS},i})^{-1}$ independently. Also, each resonator works to be in parallel. On the other hand, actual sound energy dissipated by the i-th resonator can be evaluated using FEM as [26,27]

$$\alpha^i_0 = \frac{W^i_{\mathrm{abs}}}{W_{\mathrm{in}}}, \quad (i = 1, 2, 3, \ldots, n), \tag{14}$$

where W^i_{abs} is the sound absorption power at the i-th resonator's surface, and W_{in} is the incident power to the MeAMS absorber's surface. They are respectively computed as

$$W_{\mathrm{in}} = \frac{p_0^2 S^{\mathrm{tot}}_{\mathrm{a}}}{2Z_0}, \quad W^i_{\mathrm{abs}} = \frac{1}{2}\int \mathrm{Re}(p v_x^*)\mathrm{d}S^i_{\mathrm{a}}, \tag{15}$$

where p_0 (= 1 Pa) is the incident sound pressure, $S^{\mathrm{tot}}_{\mathrm{a}}$ is the surface area of MeAMS absorber, and S^i_{a} is the surface area of i-th resonator. Note that the total absorption of MeAMS absorber α^{tot}_0 is also calculated as $\alpha^{\mathrm{tot}}_0 = (\sum W^i_{\mathrm{abs}})/W_{\mathrm{in}}$. From those theoretical and numerical foundations, we show how each resonator acts in MeAMS absorbers.

Figures 14(a), 14(b), and 14(c) respectively present theoretical and numerical α_0s of i-th resonator, which constructs MeAMS absorber, for Sample B1, B2, and B3. The black lines represent the sound absorption coefficient of MeAMS absorber. Note that the resonator of $i = 1$ has the lowest resonant frequency for respective samples, and the resonant frequencies increase for resonators with larger i. In theory, each resonator is designed so that Z^i_{MeAMS} shows a perfect absorption at a different resonant frequency. Therefore, the design principle of the proposed MeAMS absorber with two design methods is based on the use of near-perfect absorption of resonators with a series of different resonant frequencies to achieve bandpass filter-shaped near-perfect absorption. The two design methods automatically create this kind of absorption behavior in each resonator. However, FEM evaluation reveals that more than one resonators contribute at frequencies with a peak absorption. Each resonator is not a perfect absorber expressed by the specific acoustic impedance $Z^i_{\mathrm{MeAMS}} = (r_i Z^{-1}_{\mathrm{SAMS},i})^{-1}$. The contribution from resonators other than the main resonator is more significant when the spacing of resonance frequencies between resonators is narrower, such as Sample B1. This difference in individual resonator's contribution to overall absorption between theory and FEM is the reason for discrepancies in sound absorption characteristics between theory and FEM.

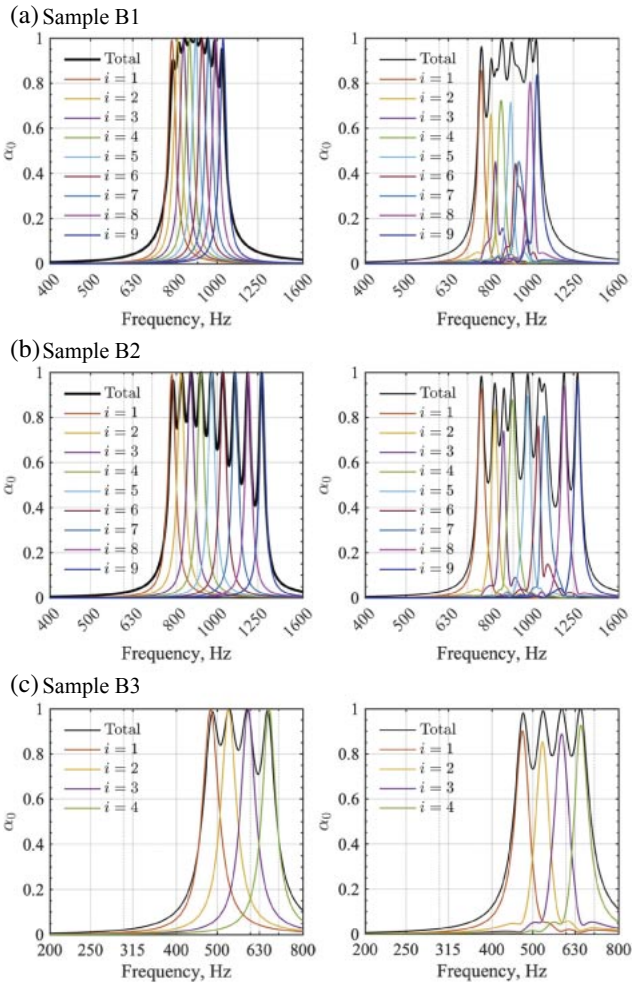

Fig. 14 The contribution of i-th resonator's absorption in the overall absorption of MeAMS absorbers (a) Sample B1, (b) Sample B2, and (c) Sample B3: (Left) Theory, (right) FEM.

To explain the multiple resonator's contribution in Sample B1, designed by Method 1, we focus on a frequency of 846 Hz. At the frequency, the total sound absorption of the MeAMS absorber is 1.0, and resonators of $i = 3$, 4, and 5, respectively, absorb 16%, 70%, and 6% of the incident acoustic wave energy. The remaining resonators absorb the remaining 8% of an acoustic wave energy. The resonator $i = 4$ is the most sound energy dissipated absorber at 846 Hz, but the two resonators $i = 3$ and 5 also have a relatively large role in absorbing about 20% sound energy. For Sample B3, designed by Method 2, the multiple resonator contribution appears at 530 Hz as an example, where the total sound absorption of the MeAMS absorber is 0.99. Therein, the resonator $i = 2$ mainly contributes to absorbing 85% of the incident acoustic wave, and the resonators $i = 1$ and 3 respectively absorb 5% and 7% of the acoustic wave energy. Although the present theory with the two design methods has a limitation regarding the precise evaluation of individual resonator's

contribution to overall absorption, it still provides a reasonable approximation of sound absorption characteristics of MeAMS absorber.

Furthermore, we can observe that resonators $i = 1$ and n with the lowest and highest resonant frequencies show a higher sound absorption than the other resonators of $i = 2, \ldots, n-1$, indicating that they are less influenced by other resonators. From this result, making the resonators $i = 2, \ldots, n-1$ have a slightly lower sound absorption coefficient than resonators $i = 1$ and n may become a simple and good design strategy to achieve more flattened absorption characteristics in MeAMS absorbers.

5.4. Design of One-third Octave Band Absorber

Finally, to further present the effectiveness of the proposed theory, we show a specially designed absorber, namely a one-third octave band absorber for room acoustics application, i.e., the reverberation control and noise reduction in a room. Two MeAMS absorbers were designed to provide near-perfect absorption at a one-third-octave bandwidth of a center frequency of 315 Hz and 500 Hz. Figure 15 shows the two one-third octave band absorbers with eight resonators for sound absorption at 500 Hz and 315 Hz bands, respectively, designated as Sample C1 and Sample C2. Method 1 was used for the design. Table 3 lists the specifications of the two absorbers. The size is $100\,\text{mm} \times 100\,\text{mm} \times H_1$. Figures 16(a) and 16(b) respectively show the Z_{MeAMS}/Z_0 and α_0 with their theoretical prediction values for Sample C1 and C2. The two absorbers show near-perfect absorption at the one-third octave bandwidth with $\bar{\alpha} = 0.91$ in Sample C1 and $\bar{\alpha} = 0.93$ in Sample C2. Also, they have sub-wavelength thicknesses of 1/22 and 1/21 for the wavelength of their lower limit frequencies. The theoretical prediction provides a reasonable approximation of the measured values.

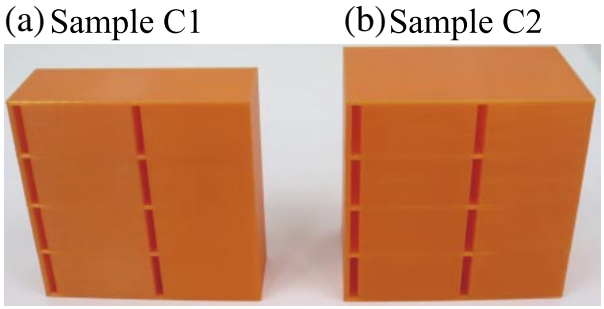

Fig. 15 One-third octave band MeAMS absorber: (a) Sample C1, (b) Sample C2.

Table 3 Specification of one-third octave band MeAMS absorbers.

Sample	n	a_1 mm	H_1 mm	d_x mm	d_1 mm	ls_1 mm
C1	8	50	35	1.2	3.2	22.5
C2	8	50	60	1.9	3.8	22.5

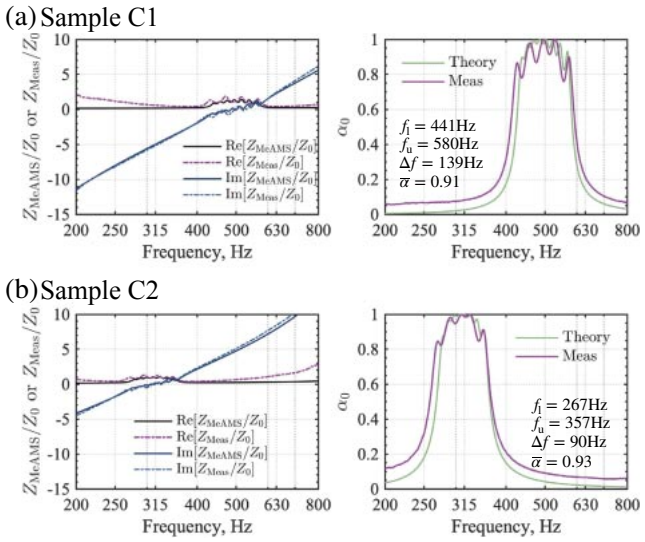

Fig. 16 Comparison of the specific acoustic impedance ratio and α_0 for two one-third octave band MeAMS absorber: (a) Sample C1, (b) Sample C2.

6. CONCLUSIONS

This paper presents the proposed sub-wavelength MeAMS absorbers for bandpass filter-shaped near-perfect sound absorption. The proposed MeAMS sound absorber is constructed as a collection of microslit-embedded single resonators, i.e., SAMS absorbers, with different resonance frequencies. The proposed two simple design methods give the component resonator's dimension in a simple manner. The design principle of the absorber is based on the assumption that each resonator with different resonant frequencies acts independently as a near-perfect absorber in parallel in the target frequencies. The verification study with FEM in Sect. 3 and the validation study with the impedance tube measurements in Sect. 4 revealed that the absorption characteristics of the SAMS absorber are predictable based on the proposed theory. We also demonstrated that two 3D-printed SAMS absorbers can achieve near-perfect sound absorption. The theory proposed in Sect. 2 is applicable to AMS absorbers with various shaped holes by changing the flow resistivity and the equivalent radius for various shaped holes, i.e., $\sigma\phi = 8\eta/\bar{r}^2$ for circular holes, $\sigma\phi = 7\eta/\bar{r}^2$ for square holes, and $\sigma\phi = 6.5\eta/\bar{r}^2$ for equilateral triangle holes [17]. The theory is one of the contributions of the present paper.

Then, the verification and validation study of MeAMS absorbers were done in Sect. 5 using the FEM simulations and the impedance tube measurements. Results revealed that the proposed theory can provide a reasonable approx-

imation of its absorption characteristics, and showed that the two design methods used to confirm the component resonator's dimension are helpful for constructing band-pass filter-shaped near-perfect absorption. Also, a numerical dissipated sound energy evaluation in individual resonators revealed that the multiple resonator's contribution exists at absorption peaks in MeAMS absorbers, especially when the resonant frequency spacing of each resonator is narrow. Therefore, the proposed simple methodology has a limitation in predicting each resonator's contribution precisely.

Regarding the absorption performance of MeAMS absorbers, an essential outcome of the present study, two 3D printed samples, B1 and B3, showed near-perfect sound absorption with an average absorption coefficient of 0.89 at the working frequency range. Their thicknesses are 18 and 20 times smaller than the wavelengths at their respective lowest frequencies. Also, at last, we presented a concept of the one-third-octave band absorber for room acoustics applications. The proposed theory could successfully design two 3D printed samples, C1 and C2, with the near-perfect absorption of $\bar{\alpha} > 0.9$ at the targeted bandwidth with sub-wavelength thickness.

ACKNOWLEDGEMENT

The author is grateful to Prof. Shinsuke Nakanishi (Hiroshima Institute of Technology, Japan) for the valuable advice related to the author's work at the Inter-Noise 2023 international conference. The authors also thank the anonymous reviewers for their helpful suggestions.

REFERENCES

[1] S. Huang, Y. Li, J. Zhu and D. P. Tsai, "Sound-absorbing materials," *Phys. Rev. Appl.*, **20**, 010501 (2023).

[2] M. Yang and P. Sheng, "Acoustic metamaterial absorbers: The path to commercialization," *Appl. Phys. Lett.*, **122**, 260504 (2023).

[3] C. Zhang and X. Hu, "Three-dimensional single-port labyrinthine acoustic metamaterial: Perfect absorption with large bandwidth and tunability," *Phys. Rev. Appl.*, **6**, 064025 (2016).

[4] S. Huang, Z. Zhou, D. Li, T. Liu, X. Wang, J. Zhu and Y. Li, "Compact broadband acoustic sink with coherently coupled weak resonances," *Sci. Bull.*, **65**, 373–379 (2020).

[5] Z. Ren, Y. Cheng, M. Chen, X. Yuan and D. Fang, "A compact multifunctional metastructure for low-frequency broadband sound absorption and crash energy dissipation," *Mater. Des.*, **215**, 110462 (2022).

[6] S. Nakanishi, "An acoustic metasurface by application of planar periodic arrays of resonators with a multiple folded long neck for broadband sound absorption," *Proc. Inter-Noise 2023*, No. 1-13-10, 10 pages (2023).

[7] C. Lagarrigue, J. P. Groby, V. Tournat, O. Dazel and O. Umnova, "Absorption of sound by porous layers with embedded periodic arrays of resonant inclusions," *J. Acoust. Soc. Am.*, **134**, 4670–4680 (2013).

[8] C. Lagarrigue, J.-P. Groby, O. Dazel and V. Tournat, "Design of metaporous supercells by genetic algorithm for absorption optimization on a wide frequency band," *Appl. Acoust.*, **102**, 49–54 (2016).

[9] M. A. Mironov and V. V. Pislyakov, "One-dimensional acoustic waves in retarding structures with propagation velocity tending to zero," *Acoust. Phys.*, **48**, 347–352 (2002).

[10] Y. Mi, W. Zhai, L. Cheng, C. Xi and X. Yu, "Wave trapping by acoustic black hole: Simultaneous reduction of sound reflection and transmission," *Appl. Phys. Lett.*, **118**, 114101 (2021).

[11] J. Li, W. Wang, Y. Xie, B. I. Popa and S. A. Cummer, "A sound absorbing metasurface with coupled resonators," *Appl. Phys. Lett.*, **109**, 091908 (2016).

[12] H. Zhao, Y. Wang, J. Wen, Y. W. Lam and O. Umnova, "A slim subwavelength absorber based on coupled microslits," *Appl. Acoust.*, **142**, 11–17 (2018).

[13] G. do N. Almeida, E. F. Vergara, L. R. Barbosa, A. Lenzi and R. S. Birch, "Sound absorption metasurface with symmetrical coiled spaces and micro slit of variable depth," *Appl. Acoust.*, **183**, 108312 (2021).

[14] G. do N. Almeida, E. F. Vergara, L. R. Barbosa and R. Brum, "Low-frequency sound absorption of a metamaterial with symmetrical-coiled-up spaces," *Appl. Acoust.*, **172**, 107593 (2021).

[15] G. do N. Almeida, E. F. Vergara, L. R. Barbosa, A. Lenzi, P. H. Mareze and R. S. Birch, "Acoustic analysis of a metasurface for normal and random incidence sound waves," *Phys. Lett. A*, **451**, 128417 (2022).

[16] T. Okuzono, T. Nitta and K. Sakagami, "Note on micro-perforated panel model using equivalent-fluid-based absorption elements," *Acoust. Sci. & Tech.*, **40**, 221–224 (2019).

[17] J. F. Allard and N. Atalla, "Sound propagation in cylindrical tubes and porous materials having cylindrical pores," in *Propagation of Sound in Porous Media: Modeling Sound Absorbing Materials*, 2nd ed. (John Wiley & Sons, Chichester, 2009), Chap. 4, pp. 45–72.

[18] D.-Y. Maa, "Theory of microslit absorbers," *Chin. J. Acoust.*, **20**, 1–10 (2001).

[19] P. Cobo and F. Simón, "Multiple-layer microperforated panels as sound absorbers in buildings: A review," *Buildings*, **9**, 53 (2019).

[20] P. Cobo, C. de la Colina and F. Simón, "On the modeling of microslit panel absorbers," *Appl. Acoust.*, **159**, 107118 (2020).

[21] COMSOL Documentation, "Pressure acoustics interfaces," in *Acoustics Module User's Guide ver. 6.1* (COMSOL, Stockholm, 2022), Chap. 2, pp. 63–172.

[22] M. Berggren, A. Bernland and D. Noreland, "Acoustic boundary layers as boundary conditions," *J. Comput. Phys.*, **371**, 633–650 (2018).

[23] ISO 10534-2:1998, Acoustics — Determination of sound absorption coefficient and impedance in impedance tubes — Part 2: transfer-function method (ISO, Geneva, Switzerland, 1998).

[24] K. Sakagami, M. Kusaka, T. Okuzono and S. Nakanishi, "The effect of deviation due to the manufacturing accuracy in the parameters of an MPP on its acoustic properties: Trial production of MPPs of different hole shapes using 3D printing," *Acoustics*, **2**, 605–616 (2020).

[25] M. Yang and P. Sheng, "Sound absorption structures: From porous media to acoustic metamaterials," *Annu. Rev. Mater. Res.*, **47**, 83–114 (2017).

[26] K. Uenishi, T. Okuzono and K. Sakagami, "Finite element analysis of absorption characteristics of permeable membrane absorbers array," *Acoust. Sci. & Tech.*, **38**, 322–325 (2017).

[27] T. Okuzono, K. Uenishi and K. Sakagami, "Experimental comparison of absorption characteristics of single-leaf permeable membrane absorbers with different backing air cavity designs," *Noise Control Eng. J.*, **68**, 237–245 (2020).